



## ENGINEERING

# Transparent organic upconversion devices displaying high-resolution, single-pixel, low-power infrared images perceived by human vision

Chun-Jen Shih<sup>1,2</sup>, Yu-Ching Huang<sup>2,3</sup>, Tai-Yung Wang<sup>2,3</sup>, Chang-Wei Yu<sup>2</sup>, I-Sheng Hsu<sup>2</sup>, Abdul Khalik Akbar<sup>2</sup>, Jai-Yi Lin<sup>2</sup>, Sajal Biring<sup>2</sup>, Jiun-Haw Lee<sup>1\*</sup>, Shun-Wei Liu<sup>2\*</sup>

Crystalline photodiodes remain the most viable infrared sensing technology of choice, yet the opacity and the limitation in pixel size reduction per se restrict their development for supporting high-resolution in situ infrared images. In this work, we propose an all-organic non-fullerene-based upconversion device that brings invisible infrared signal into human vision via exciplex cohost light-emissive system. The device reaches an infrared-to-visible upconversion efficiency of 12.56% by resolving the 940-nm infrared signal (power density of 103.8  $\mu\text{W cm}^{-2}$ ). We tailor a semitransparent (AVT,  $\sim 60\%$ ), large-area (10.35  $\text{cm}^2$ ), lightweight (22.91 g), single-pixel upconversion panel to visualize the infrared power density down to 0.75  $\mu\text{W cm}^2$ , inferring a bias-switching linear dynamic range approaching 80 dB. We also demonstrate the possibility of visualizing low-intensity infrared signals from the Face ID and LiDAR, which should fill the gap in the existing technology based on pixelated complementary metal-oxide semiconductors with optical lenses.

## INTRODUCTION

Infrared visualization technologies have received much attention because they aim to extend human sensation beyond visible spectra, finding potential applications such as night-vision goggles in military combat, in vitro intraoperative diagnoses (1), and revealing potential risks at night (2). However, despite the promising benefits, the mainstream crystalline materials such as silicon and compound semiconductors failed to visualize infrared information without interrupting our intrinsic vision (Fig. 1A). It has struggled to support high-resolution large-area images relying on complementary metal-oxide semiconductor (CMOS) that requires delicate lithographic techniques (3). In addition, it has raised concerns that pixel size reduction without sacrificing geometric cross-talk and fill factor hiked up the fabrication costs (4). Extensive research has been devoted to exploring large-area, low-noise, low-cost, and transparent photodetection alternatives to circumvent the trade-offs in existing technology (5, 6).

Infrared-to-visible upconversion devices [the compact stacking of infrared sensing photodetector in conjunction with visible light-emitting diode (LED)] offer an attractive prospect of reifying infrared images into vision at a relatively low cost, i.e., a high-quality pixel-free infrared image can be realized without high-density readout integrated circuits. In the past decade, the photon-to-photon upconversion efficiency ( $\eta_{\text{p-p}}$ ), a leading figure of merit assessing the infrared photon utilization rate on quantum efficiency, has witnessed remarkable growth from 0.2% addressing the lattice mismatch issue with the hybrid heterogeneous interface (7) to 25.52% based on an all-organic structure with single photoactive component (fig. S1) (8). In particular, organic upconversion

devices (OUDs) demonstrated alluring advantages compared to their inorganic counterparts (9), including three-dimensional visualization (10), full-color versatility (11), flexible to substrate deformation (12), high-resolution image (8), and see-through display (8, 13), and have been applied in wellness monitoring (14) and biological imaging (15–18).

Besides enforcing the intermolecular  $\pi$ - $\pi$  stacking by the side-chain decoration in the polymeric donor to achieve a high absorption coefficient toward the longer wavelength (19), much attention has been paid to developing non-fullerene acceptors (NFAs) with delicate molecular design recently (20, 21). They demonstrated diversified optoelectrical properties and structure-property relationships, such as high carrier mobility comparable to that of the existing donor materials, tunable miscibility with the donor for desirable phase mixing while retaining enough domain purity for carrier extraction in the bulk heterojunction (BHJ) blend, and above all, a high extinction coefficient stretching into the near-infrared (NIR) region via tailored electron push-pull hybridization segments. Although encouraging efforts were made by implementing infrared-sensitive NFAs in the charge generation layer (CGL) (17, 22), concern exists before carving a niche for NFA-based OUDs. Practically, the direct vacuum deposition of an organic LED (OLED) on the solution-processed BHJ blend was adopted in most literature concerning the favorable optical resonant and free-from-solvent orthogonality issue. However, unlike desired complementary absorption spectra covering solar energy to create a channel-II photoexcitation process in photovoltaics (21, 23), the spectral overlap of the broadband CGL absorption with the emitter quenched the out-coupled visible light in opaque OUDs end-capped with a reflective metal electrode, lowering detectivity and efficiency in general. While introducing more light-emitting sub-units mitigated the reabsorption loss (12), it complicated the overall device stacking. It remains to be explored whether the NFA-based OUD can be applied for large-area weak-light sensing applications that most studies imposed intense monochromatic

<sup>1</sup>Graduate Institute of Photonics and Optoelectronics and Department of Electrical Engineering, National Taiwan University, Taipei 10617, Taiwan. <sup>2</sup>Organic Electronics Research Center and Department of Electronic Engineering, Ming Chi University of Technology, New Taipei City 24301, Taiwan. <sup>3</sup>Department of Materials Engineering, Ming Chi University of Technology, New Taipei City 24301, Taiwan.

\*Corresponding author. Email: jiunhawlee@ntu.edu.tw (J.-H.L.); swliu@mail.mcut.edu.tw (S.-W.L.)

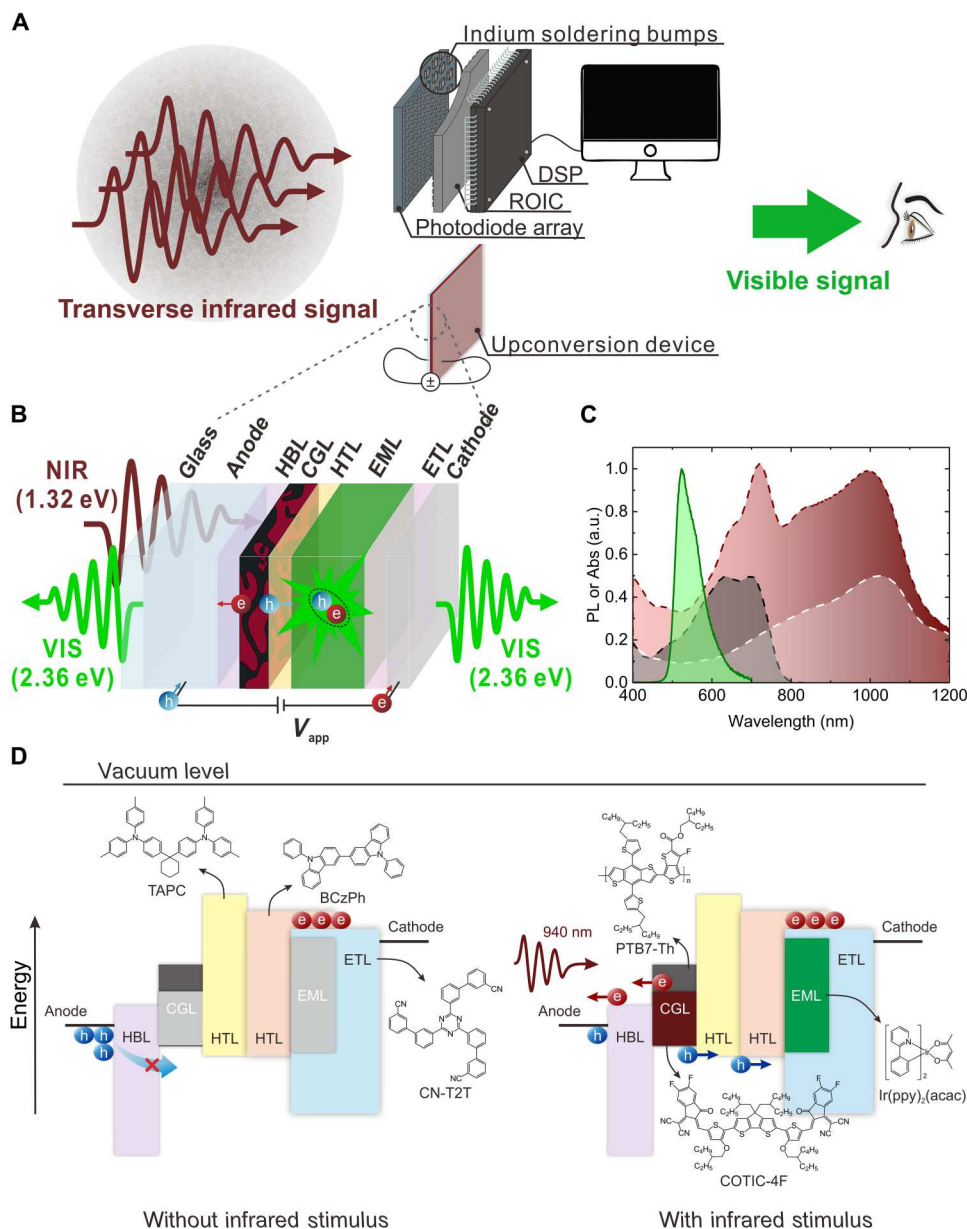


**Fig. 1. Schematic illustration of infrared visualization process.** (A) Operational mechanisms between conventional infrared imaging and the see-through pixel-free upconversion approach. The noise covering the infrared signal implies that the pattern can be identified at night or under adverse weather conditions. ROIC, readout integrated circuit. DSP, digital signal processor. (B) Infrared-to-visible upconversion process of the proposed OUD with the stacking cross section (not scale to size between blocks). (C) Normalized absorption spectra of PTB7-Th (black dash line), COTIC-4F (white dash line), and PTB7-Th:COTIC-4F (red dash line) solid-state thin films and the spectral photoluminescence (PL) of the Ir(ppy)<sub>3</sub> emitter (green solid line) dispersed in BCzPh:CN-T2T mixing blend in arbitrary units (a.u.). (D) Energy band diagram of the OUD device in the absence/presence of an infrared stimulus (flat band potential). Each block represents the frontier orbitals of the material with molecular structure inset (not to scale).

infrared light on a confined area with barely satisfactory luminance (fig. S1).

Beyond the challenge involved in the current image sensors, the top emissive upconversion device is expected to achieve the true potential of extending human vision without pixelation. The concept was first validated by Kim *et al.* (9) with the multispectral digital single-lens reflex camera equipped with an infrared-sensitive upconversion component. The ability to visualize three-dimensional images of both reflective and nonreflective objects was further

verified later on (10). The cancerous tissue of a mouse breast sample can be clearly identified from the normal tissue by the *in vivo* bioimaging with sharper contrast compared to the image captured by an infrared camera (18). However, these previous works on upconversion images were sequentially collected and processed by a standard camera based on a charge-coupled device or CMOS sensors equipped with bulky optical lenses, which failed to perceive infrared images by the naked eye (7–10, 15–18). Challenges called

for a novel upconversion design to in situ visualize high-resolution, large-area, low-intensity infrared images without pixelation.

## RESULTS

### Design rationale and operational mechanism

To tackle these issues, we proposed a semitransparent, large-area, all-organic infrared upconversion device, selectively resolving infrared light density down to submicrowatt per square centimeter (Fig. 1B). A narrow-bandgap NFA of COTIC-4F ( $E_g$  of 1.10 eV) with an acceptor-donor-acceptor (A-D'-D-D'-A) chemical configuration was used (24, 25), developing BHJ blend (3:2 in weight) with a typical low-bandgap conjugated copolymer (PTB7-Th) as the CGL, expanding the absorption spectrum comparable to that of a standard silicon photodiode (Fig. 1C). Note that the BHJ thin film with a thickness of 70 nm followed a minimum absorption at the wavelength of 520 nm, which could alleviate the efficiency loss of upconversion luminance peaked at 523 nm in principle (12).

The energy band diagram of the device stacking is presented in Fig. 1D. To suppress the leakage current in the absence of infrared stimulation, a strong n-type composite of zinc oxide (ZnO) was prepared via sol-gel method as the hole blocking layer (26) modified with the polyethylenimine ethoxylated (PEIE) for decoupling electrostatic interaction at the contact (27). We inserted 1,1-bis (di-4-tolylamino-phenyl) cyclohexane (TAPC) bridging the CGL and the emissive layer as the hole transporting layer not because of

energetic level alignment minimizing contact barrier but on account of the charge selectivity repelling minority carriers (electron) (14, 28). Namely, we expected interfacial modification playing a pivotal role in suppressing nonradiative surface recombination loss from minority carriers. It has been argued that a low turn-on voltage of the upconversion process can be fulfilled by the OLEDs harnessing the exciplex system (8), meeting the need for low-power consumption purposes. Therefore, a bipolar exciplex showing ionic polarization behavior was formed by blending 9,9'-diphenyl-9H,9'H-3,3'-bicarbazole (BCzPh) with the electron transporting layer (ETL) 3',3'',3''-(1,3, 5-triazine-2,4,6-triyl)tris([1,1'-biphenyl] 3-carbonitrile) (CN-T2T) (29, 30) to cohost the bis (2-phenylpyridine)iridium(III)-acetylacetonate [Ir(ppy)<sub>2</sub>(acac)] phosphorescent emitter as the emission layer (EML), which demonstrated efficient exciton relaxation with trivial charge carrier pile-up dynamic in our previous study (8, 30). In the absence of infrared stimulus, the built-in potential between the BHJ interface of BCzPh:CN-T2T exciplex cohost limits the electron hopping, while no hole carriers were generated from the CGL. Therefore, an electron-rich scenario was created in the EML, where most of the electrons accumulated as the phosphorescent emitter acting as a deep trap that enforced the electron in the EML (31). In the presence of an infrared stimulus, photoinduced hole carriers travel to the EML guided by the external field for charge recombination. To selectively band-pass the upconversion visible light while harnessing incident infrared photon, a semitransparent copper-silver alloy thin

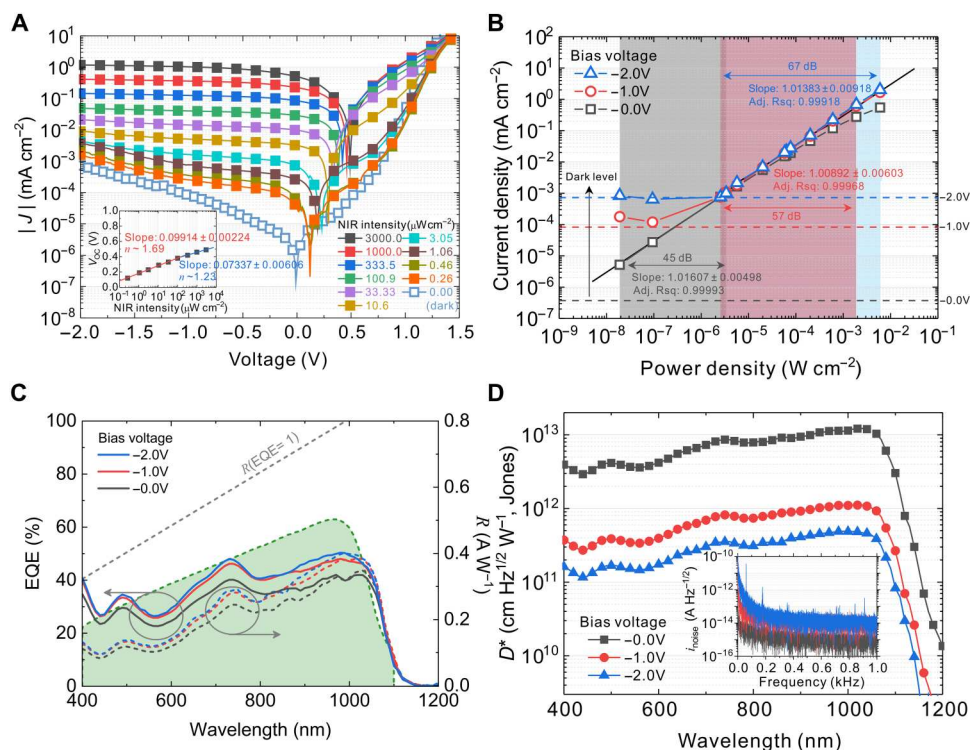


**Fig. 2. Device performance of the PTB7-Th:COTIC-4F OPD.** (A) Absolute current density–voltage characteristics of the device under various intensities of 940-nm laser illumination. The inset shows that the  $V_{OC}$  depends on the NIR intensity with two-step linear fitting results. (B) LDR concerning different bias voltages. The dash lines represent the bias-dependent dark level, retrieved from (A) for reference. The solid black line represents the ideal case (slope equals one). (C) External quantum efficiency (EQE) and responsivity spectra of the device under different bias voltages. The responsivity of a standard silicon photodiode (FDS100, Thorlabs) is recorded for reference (olive). (D)  $D^*$  spectra of the device operated at different bias voltages. The inset shows the noise current under different bias voltages. The spike noises are attributed to the instrumental hum.

film (Cu:Ag, 1:50) (32) capping with  $\text{WO}_3$  layer was introduced as the top cathode to preserve an average visible transmittance (AVT) approaching 60% for the overall device stacking.

### Infrared photodetection

We first evaluated the performance of PTB7-Th:COTIC-4F CGL based on the organic photodetector (OPD) structure (Materials and Methods), as demonstrated in Fig. 2. The OPD showed consistent responsivity with infrared power density ranging from  $3.0 \text{ mW cm}^{-2}$  to  $0.26 \text{ } \mu\text{W cm}^{-2}$ . The dark current interfered with the low-intensity response ( $<3.05 \text{ } \mu\text{W cm}^{-2}$ ) beyond the bias voltage of  $-1.0 \text{ V}$  (Fig. 2A), which can be regarded as the increased shot noise and the energy barrier lowering from reverse DC bias. It should be emphasized that the two-step logarithmic dependence of the open-circuit voltage ( $V_{\text{OC}}$ ) on the incident intensity ( $V_{\text{OC}} \propto \frac{nk_B T}{q} \ln P$ ) suggested the transition between bimolecular and nonradiative Shockley-Read-Hall recombination losses with an ideality factor ( $n$ ) of 1.23 and 1.69 (33), respectively (inset in Fig. 2A). It has been advised that trap-assisted generated charges through intragap states act as primary mechanism governing the dark current, as evidenced in donor-acceptor blend systems (34).

The linear dynamic range (LDR), the operational window of the photoactive sensors expressed as  $\text{LDR} = 20 \log (P_{\text{max}}/P_{\text{min}})$  in units of decibel, evaluates the device detectivity on varying incident light intensity ( $P_{\text{max}}$  and  $P_{\text{min}}$  are the upper and lower limit of power densities while keeping responsivity linear). It is essential to characterize the authentic LDR approaching the noise equivalent power (NEP) in a Faraday cage against undesired noise (35). Although the current density deviated from linear at the low-power region under bias other than zero (Fig. 2B), overwhelmed by the shot noise-dominated dark level, an LDR of 67 dB was achieved at  $-2.0 \text{ V}$  as the power density decreased to  $2.54 \text{ } \mu\text{W cm}^{-2}$ . The high linearity with a slope close to ideal ( $1.01383 \pm 0.00918$ ) suggests an ohmic contact with negligible series resistance, while the nonideal divergence cases in the high-power region are caused by the bimolecular recombination loss and space charge effect of the large mobility difference in the BHJ blend ( $\mu_n/\mu_e = 48$ , as revealed by Vollbrecht *et al.*) (36, 37). Although the lower limit (close to NEP) can be established by further attenuating the light intensity and introducing a lock-in amplifier or spectrum analyzer (38), it would be beyond the limit of the upconversion luminance and human sensation.

The external quantum efficiency (EQE) was recorded to assess the charge generation ability toward the chopped monochromatic infrared light (Fig. 2C). A broadband response stretching cut-off wavelength beyond 1000 nm provides an appealing potential for biomedical applications. A decent value of 37.84% at the wavelength of 1050 nm was achieved without external bias despite a relatively small highest occupied molecular orbital offset between PTB7-Th and COTIC-4F (25). The low field-dependent responsivity suggests minor geminate recombination loss under bias in the BHJ blend. Note that the maximum responsivity ( $0.4 \text{ A W}^{-1}$ ) is one of the most efficient OPDs in the NIR frequency and comparable to the finest silicon photodiode thanks to the sophisticated molecular design (24). The specific detectivity ( $D^*$ ), a unified metric that quantifies the sensitivity toward the weak light signal of a photodetector, can therefore be deduced from  $D^* = R\sqrt{A\delta f}/i_{\text{noise}}$ , which depends on the responsivity ( $R$ ), active area ( $A$ ), measurement

bandwidth ( $\delta f$ ), and the overall noise of the device ( $i_{\text{noise}}$ ). An ultrahigh  $D^*$  of  $1.08 \times 10^{13} \text{ cm Hz}^{1/2} \text{ W}^{-1}$  (Jones) at the wavelength of 940 nm was achieved in the self-powered mode without external field (25), where the spontaneous thermal noise dominated via ambient temperature agitation (fig. S2) (5). Although the increased shot noise under bias caused the  $D^*$  to plunge, the capability of identifying faint NIR light (780 to 1150 nm) with PTB7-Th:COTIC-4F BHJ had been verified with a decent  $D^*$  exceeding  $10^{11}$  Jones at the bias voltage of  $-2.0 \text{ V}$ . Therefore, we can conclude that PTB7-Th:COTIC-4F is a promising CGL candidate for the up-conversion device. Detailed information on the OPD characterization can be found in the Supplementary Materials (Supplementary Text and table S1).

### Infrared visualization

The infrared photon can be figured with the thin-film deposition of an OLED on the BHJ blend accordingly (Materials and Methods). Further characterization of 30 individual OLED pixels was summarized in the Supplementary Materials (fig. S3). Figure 3 reveals the upconversion performance of the PTB7-Th:COTIC-4F OUD with the standard cathode structure. A saturated upconversion luminance of  $337.2 \text{ cd m}^{-2}$  can be obtained concerning the infrared power density of  $1.0 \text{ mW cm}^{-2}$  at the bias voltage of 8.0 V (Fig. 3, A and B), where limited visible light can be found in the absence of an infrared stimulus (fig. S4). The strong correlation between the infrared intensity and the upconversion luminance substantiated the strategy of using BCzPh:CN-T2T cohost phosphorescence light-emissive system (8). The bipolar exciplex blend generating spin-orbital coupling for intermolecular charge transfer could harness the nonradiative triplet excitons and facilitate the energy transfer toward the phosphorescent emitter (39). It was advised that the subgap turn-on voltage ( $2.0 \text{ V}$  at  $0.1 \text{ cd m}^{-2}$ ), which is lower than the bandgap energy of the emitter [ $2.37 \text{ eV}$  of  $\text{Ir}(\text{ppy})_2(\text{acac})$  in our case] could be assigned to the photovoltaic effect of the CGL (40). Note that it usually requires more than 100 nm of BHJ thickness to balance the trade-off between sufficient infrared photons and charge collection for upconversion luminance (22), while less than 70 nm of the PTB7-Th:COTIC-4F BHJ blend should meet the balance in our work (fig. S5). The linear response of the upconversion luminance with respect to the infrared power density can be examined by the  $\text{LDR} = 20 \log (P_{\text{max}}/P_{\text{min}})$  once again, focusing on the contrast ratio of the image quality (Fig. 3C). We set the lower limit as  $0.1 \text{ cd m}^{-2}$  to conform with the turn-on luminance defined in most literature. The device demonstrated a constant responsivity tracking power density with almost four orders of magnitude (from  $1.0 \text{ mW cm}^{-2}$  to  $0.52 \text{ } \mu\text{W cm}^{-2}$ ) under various bias voltages. Whereas the low-intensity response deviated from the ideal, ascribed to the perturbation of leakage luminance, the luminance short at the high-intensity region can be assigned to the bimolecular recombination, as suggested in Fig. 2B. Nevertheless, an LDR of 36 dB can be preserved at a bias voltage of 4.0 V, stretching down to the intensity of submicrowatt per centimeter square. Hence, we suppose that a wide-range operation of OUD (LDR span more than five orders of magnitude) is plausible by modulating the applied voltage as a function of incoming signal intensity.

The spectral selectivity and light emission behaviors of the OUD were further explored from the perspective of EQE and current efficiency, respectively. The OUD presented an EQE of more than

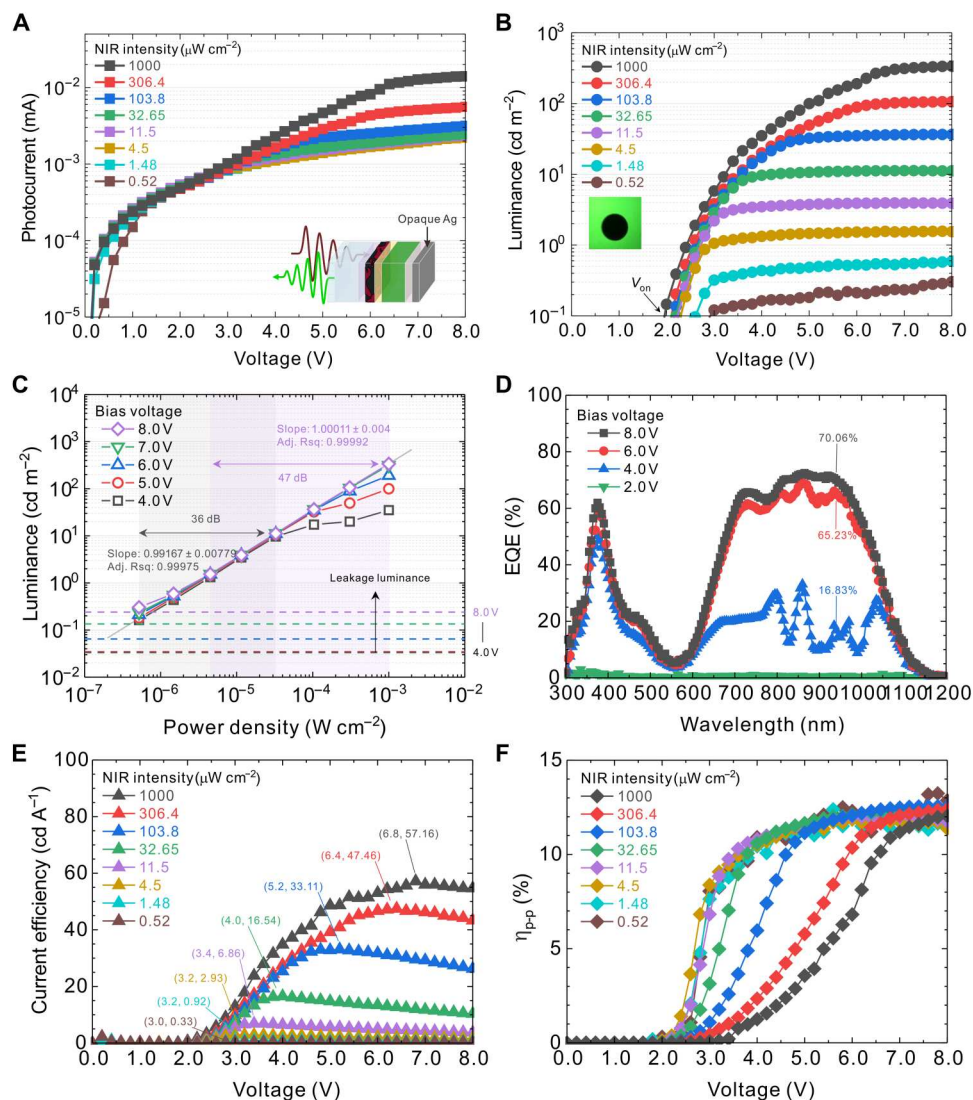


**Fig. 3. Device performance of the PTB7-Th:COTIC-4F OUD (standard structure).** (A) Current density–voltage characteristics as a function of 940-nm laser intensity. (B) Upconversion luminance of the device upon the same infrared stimulus. The inset shows the photo of the pixel under operation. (C) LDR of the upconversion luminance at different bias voltages. The dash lines represent the bias-dependent leakage luminance (without infrared illumination). The solid gray line represents the ideal case (slope equals one). (D) EQE spectra of the device under different bias voltages. (E) The current efficiency of the device under various infrared power densities. (F) The infrared-to-visible upconversion efficiency of the device under various infrared power densities.

70% at the wavelength of 940 nm under an external bias voltage of 8.0 V (Fig. 3D), while a suppressed value lower than 7% was recorded at the peak electroluminescent wavelength of the upconversion luminance. The spectral selectivity for incident energy signifies the suitable optical path constructed in favor of visible light out-coupling. The higher EQE found in the OUD than that of OPD (saturated around 50%) can be rationalized as follows. First, the non-fullerene BHJ photovoltaic suffers from nongeminate recombination dynamics, where undesirable bimolecular and surface trap-assisted recombination dominate (41). Both recombination losses were observed in the PTB7-Th:COTIC-4F system under this study (36). Second, it has been elaborated that poor charge selectivity is the main contributor to nonradiative recombination loss ascribed to the direct contact between the molybdenum oxide ( $\text{MoO}_3$ ) and the BHJ blend (42). In the proposed OUD, the charge selectivity of

TAPC should mitigate the surface recombination loss and the space charge effect due to the substantial mobility difference of the BHJ blend (36). Third, the charge-blocking character of the exciplex-based EML allows us to impose a more substantial bias for charge extraction. Note that no EQE was recorded from the OUD under the bias voltage lower than 2.0 V, unlike that observed in OPD, because the photoinduced hole carriers were consumed only if enough carriers were guided toward the EML for recombination (cf. Fig. 1D), i.e., we operated the upconversion device when both enough infrared illumination and electrical field were satisfied. The voltage corresponding to the maximum current efficiency shifted (from 6.8 to 3.0 V as labeled) as the incident intensity decreased (Fig. 3E), suggesting the reconciliation process finding optimal charge balance between the external bias and CGL for exciton relaxation. Although the current efficiency experienced a minor roll-off

as increasing the bias voltage, a reverse trend was found in the  $\eta_{p-p}$  rate (Fig. 3F).

The upconversion performance can be estimated by the EQE product of the infrared photodetector and the LED, respectively, or as a whole (43). For example, Hu *et al.* (44) recently demonstrated a  $\eta_{p-p}$  of 0.16% with an EQE product of 0.29% from the OPD (10%) and OLED (2.89%) subunits. Yang *et al.* (12) achieved a record-high  $\eta_{p-p}$  of 29.6% with an EQE of 61.7% from the CGL and an ultrahigh EQE of 50% from the tandem OLED. In our case, an estimated EQE product of 12.85% was deduced from the OPD (~50% in Fig. 2C) and the exciplex cohost phosphorescent OLED (25.7% in fig. S3). Here, the EQE difference between the OLED single units and the electron-to-photon rate of the OUD (~20% in fig. S6) may be attributed to the unbalanced charge carrier in the EML of OUD. In the upconversion process, the hole carriers are supplied with the CGL

after an infrared stimulus (Fig. 1D). An ideal charge balance scenario may be restored once a proper amount of photoinduced hole carriers is introduced into the EML. Overall, it makes sense that one would realize high efficiency from the OUD if the EQE of both subunits is optimized in the integrated device. Nevertheless, it is necessary to emphasize that the accurate  $\eta_{p-p}$  should be derived from direct measurement of monolithic OUD instead of the EQE product between individual subunits. We carefully quantified the incident infrared power density and the upconversion luminance against overestimation as follows. First, the maximum  $\eta_{p-p}$  rate was calculated by excluding the contribution from the dark current, which conforms to the photoinduced upconversion luminance in the actual case. Second, unlike most studies that characterized the upconversion luminance via a luminance meter or spectroradiometer, assuming that the light emission source is a Lambertian emitter,

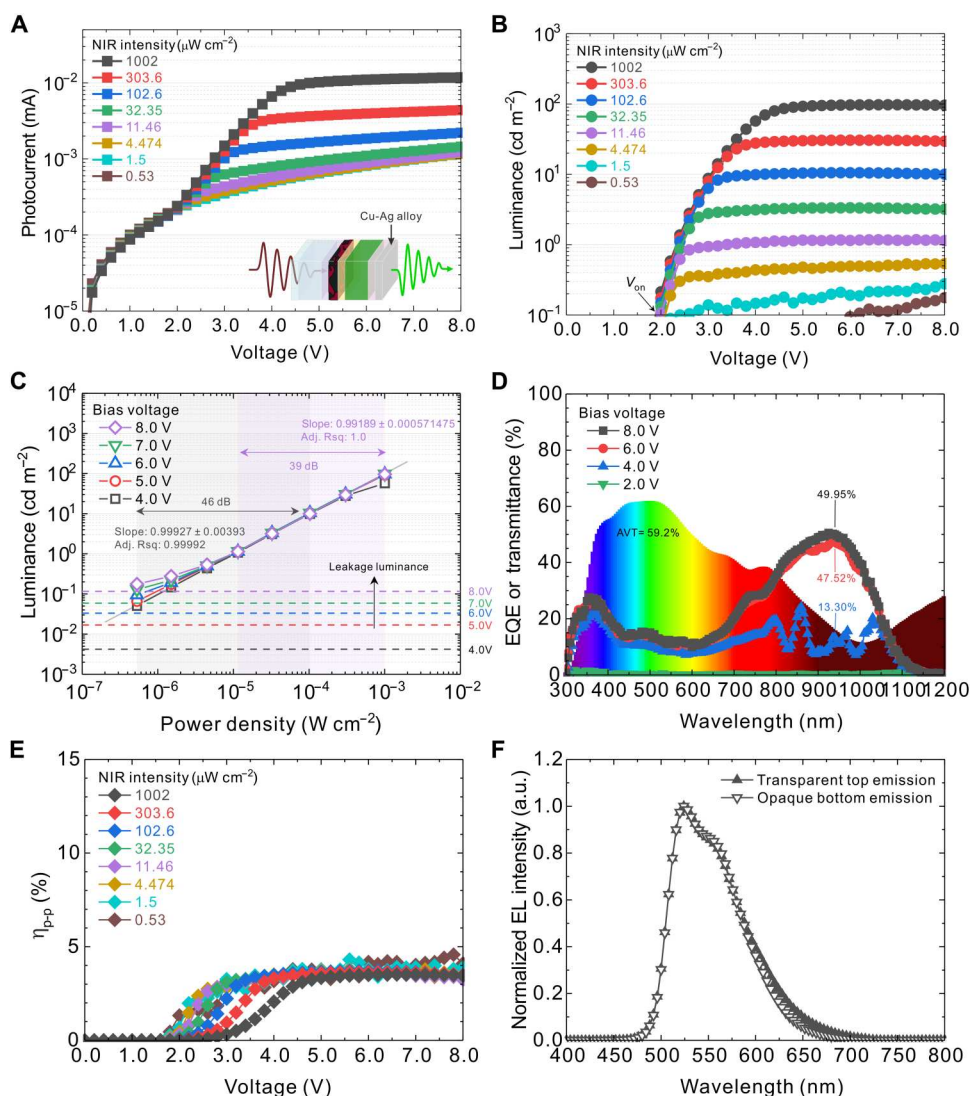


**Fig. 4. Device performance of the PTB7-Th:COTIC-4F OUD (top emission).** (A) Current density–voltage characteristics as a function of 940-nm laser intensity. (B) Upconversion luminance of the device upon the same infrared stimulus. (C) LDR of the upconversion luminance at different bias voltages. The dash lines represent the bias-dependent leakage luminance (without infrared illumination). The solid gray line represents the ideal case (slope equals one). (D) The transmittance spectrum (rainbow waterfall) and EQE spectra recorded from the semitransparent top cathode. (E) The infrared-to-visible upconversion efficiency of the device under various infrared power densities. (F) Normalized electroluminescent spectra of the top-emissive OUD and OUD in standard structure (Fig. 3).

we collect the upconversion luminance from the integrated sphere (18). Third, to prevent the extra photocurrent contributed by the CGL outside the overlapping area defined by the anode and cathode upon infrared excitation, a phenomenon found in most solid-state thin-film solar cells, we have used a shadow mask (size covering the whole sample in case of light piping) to exclusively define the active area following the commentary proposed by Snaith (45). As a result, a maximum infrared-to-visible  $\eta_{p-p}$  of 12.56% can be achieved by reducing the incident infrared power density down to  $103.8 \mu\text{W cm}^{-2}$ , at which the device showed the maximum electron-to-photon rate (fig. S6). More information about the characterization protocols can be found in Materials and Methods.

### Top-emissive infrared visualization

The ability to visualize low-intensity infrared light had been systematically examined in PTB7-Th:COTIC-4F OUD with the standard reflective cathode. Despite holding great promise, how much the upconversion luminance, or the deduced  $\eta_{p-p}$ , can be preserved after comprising a semitransparent top-emissive cathode remains crucial. Because a semitransparent metal alloy alleviates the surface scattering loss from localized plasmon resonance effect in the NIR region (32), we replaced the standard Ag cathode (100 nm) with Cu:Ag alloy thin film (12 nm) capped with the index-matching  $\text{WO}_3$  layer for the top-emissive structure. Although further reducing the alloy thickness can, on the one hand, achieve higher transmittance in visible frequency, it undermines the wavelength selectivity for the reflective infrared signal, as well as the uniformity concern on the other hand. Hence, an AVT approaching 60% was achieved by the overall device stacking (Fig. 4). The device managed an EQE of 49.95% at the wavelength of 940 nm under an external bias voltage of 8.0 V with a transmittance loss of 15.14% at the same wavelength (Fig. 4D). As a matter of fact, Cu:Ag alloy cathode reflected only partial incoming infrared photons, and more than half of the upconversion luminance was released from the indium tin oxide (ITO) anode (i.e., favorable AVT of typical ITO substrate for visible light out-coupling). The efficiency of the top-emissive device was three times smaller than the standard structure, accounting for a maximum  $\eta_{p-p}$  of 3.7% after excluding the luminance under dark (Fig. 4E). Although the loss can be restored by increasing the CGL thickness and selectively regulating the light path (9), we constructed the transparent device following the standard device for consistency. Besides, the transparency of the device can be lost after integrating a cold mirror. The top-emissive device could track the infrared power density down to submicrowatt per centimeter square level in linear (Fig. 4C) with an electroluminescent spectrum similar to that of the standard device (Fig. 4F).

We thus demonstrated a lightweight (22.91 g in total) and large-area ( $10.35 \text{ cm}^2$ ) single-pixel upconversion panel to investigate the possibility of visualizing infrared images without optical lens or cameras (Fig. 5). A commercial infrared detection card was taken as the reference sample to evaluate the LDR response of the large-area upconversion panel. The applied bias was tuned (4.0 to 8.0 V) to catch the incident infrared power density ranging almost four orders of magnitude, accounting for a 77.99 dB in terms of a bias-switching LDR. The top-emissive upconversion panel generated clear and uniform large-area upconversion luminance, revealing the infrared power density down to  $0.75 \mu\text{W cm}^{-2}$ , whereas the

commercial detection card showed imperceptible brightness in this region. Note that a more precise image in the low-intensity range can be obtained by changing the structured light. However, we kept the same condition throughout the LDR measurement to show consistency between the insets. In addition, the upconversion luminance saturated at the high-intensity range. Increasing the CGL thickness or imposing a higher bias voltage could be taken into account to address this issue. Overall, we concluded that the proposed top-emissive PTB7-Th:COTIC-4F OUD should meet the need for large-area low-energy infrared visualization by the naked eye, filling the gap in the existing technology. Detailed information on the experimental setup and the large-area panel is found in the Supplementary Materials (fig. S7).

### Proof-of-concept demonstrations

Individual privacy is under threat for public information gathered by monitoring our daily activities with ever-cheaper closed-circuit television in modern society. Although dim red light can be discriminated for most camera models deployed in public (peak wavelength at 850 nm), the infrared lights entirely outside the visible range used in the camera system developed for facial recognition (peak wavelength at 940 nm) could not be distinguished. Unlike the invalid audio recording of individuals without their permission, the lack of clear consensus limitation on cameras urges us to develop wearable antidetection panels against these intrusive lights without notice. We demonstrate the ability to unveil invisible infrared light of the facial recognition technology (Face ID; Fig. 6, A to D) or light detection and ranging (LiDAR; Fig. 6, E to H) function from the single-pixel, large-area upconversion panel.

The TrueDepth camera system, primarily consisting of a proximity sensor, a flood illuminator, a dot projector, and an infrared camera, was first available on the market in late 2017 to construct the three-dimensional facial features of the smartphone user. The geometric pattern is enrolled as the biometric authentication to access the smartphone. The subject is first illuminated by the successive infrared flash from the flood illuminator, designed to work even in total darkness. The mathematical model of the face morphology is then built by recording the reflected infrared dots produced by the dot projector with the infrared camera. Before switching on the antidetection panel (Fig. 6B), an eye image of the subject behind the semitransparent panel can be identified even under low background lighting. Real-time, uniform, large-area upconversion luminance in response to the invisible infrared illumination ( $\sim 100 \mu\text{W cm}^{-2}$  produced by the flood illuminator) is captured once the power switch is turned on (Fig. 6C). Following the infrared beams projected from the dot projector, a grid of uniformly distributed infrared light spots is precisely restored to sight (Fig. 6D), pointing out the high-contrast, high-resolution superiority of the all-organic upconversion panel (8). The full version of the screen recording video is available in the Supplementary Materials (movie S1).

The great success of the highly accurate infrared sensing technology has been further integrated into the rear camera in the latest smartphone models. Besides improving focus speed under darkness with the night portrait mode, the detailed indoor space can be meshed out by measuring the traveling time of the individual reflected infrared photons from the surrounding. The visible image of a man waving while holding the smartphone can be found through the semitransparent panel (Fig. 6F), albeit the focus is

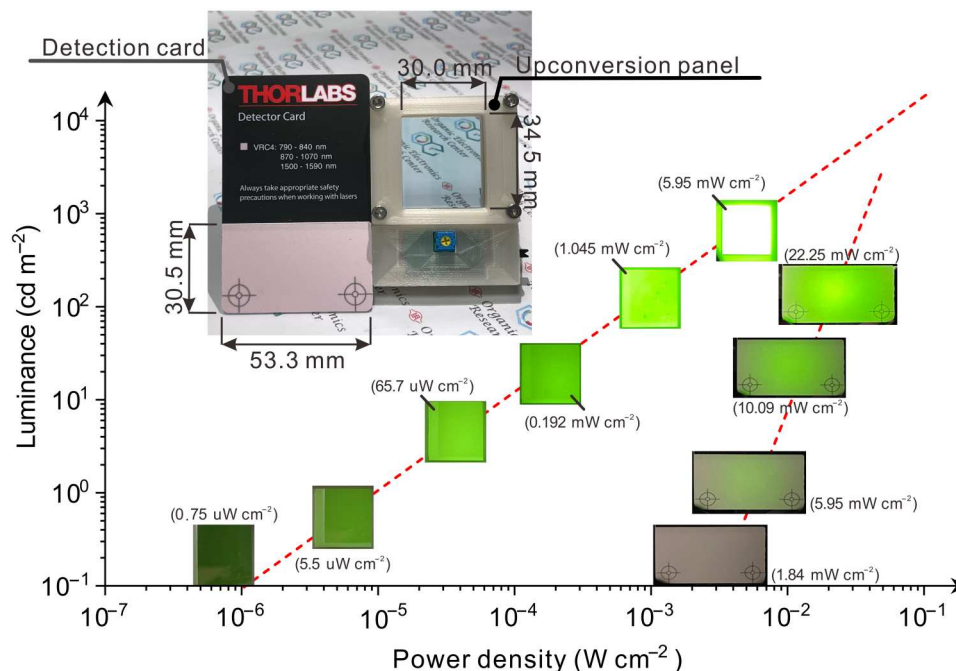


**Fig. 5. Infrared viewing sensor.** LDR comparison between the semitransparent large-area OUD and a standard infrared detection card in response to various 940-nm signal intensities. Red dashed lines are guides for the eye. The inset shows the photograph of the two infrared visualizers labeled with the active area size. Detailed OUD layout and measurement setup can be found in the Supplementary Materials.

locked on the active area of the panel and under low background lighting. Similar to the facial recognition technology at a closer range, four clear infrared light dots ( $\sim 150 \mu\text{W cm}^{-2}$ ) are included in the active area after turning on the upconversion panel power (Fig. 6G), flickering to scan the surrounding depth profile (see movie S2 for full demonstration). By extending the infrared traveling range ( $\sim 1.5 \text{ m}$ ), one single infrared light beam ( $\sim 50 \mu\text{W cm}^{-2}$ ) can be recognized with a honeycomb pattern (Fig. 6H), while the background image can be simultaneously perceived. This is the first time an infrared image can be identified by the naked eye more than one and a half meters away without any optical lens or CMOS sensors. Note that weak-light sensing (lower than  $1.0 \mu\text{W cm}^{-2}$ ) can be further achieved by approaching the maximum detection range of the LiDAR function, commensurate with the LDR measurement tracking the infrared power density down to submicrowatt per centimeter square (Fig. 5). The complete demonstration of attenuating the infrared intensity can be found in the Supplementary Materials (movie S2).

## DISCUSSION

It is a great challenge to achieve a perceivable upconversion luminance relying on the semitransparent top-emissive structure. Whether the see-through device can serve as an infrared visualization technology resolving low-intensity signals remains an unsolved puzzle. To address this issue, a state-of-the-art infrared photoactive blend (PTB7-Th:COTIC-4F) was implemented as the CGL with the collaboration of BCzPh:CN-T2T exciplex cohost phosphorescence light-emissive systems for an all-organic upconversion device. The PTB7-Th:COTIC-4F OPD demonstrated excellent detectivity for low-intensity infrared signals supporting the BHJ blend as a

promising CGL ( $D^*$  of more than  $10^{11}$  Jones in the wavelength of 780 to 1150 nm).

The PTB7-Th:COTIC-4F OUD achieved a high  $\eta_{\text{p-p}}$  of 12.56% for the standard cathodic structure based on the following factors: (i) The dark level had been substantially suppressed with the ZnO-PEIE composite. (ii) Nonradiative loss from minority carriers has been hampered by the carrier selectivity of the TAPC, and (iii) exciplex cohosting the phosphorescent emitter facilitated the radiative recombination for upconversion luminance. In the absence of infrared illumination, both the ZnO-PEIE and TAPC act as unipolar charge-transporting layers against any unwanted minority carriers. In the presence of the stimulus, the exciplex system expedites the charge recombination with a turn-on voltage lower than the bandgap energy of the emitter.

We have validated the possibility of tracking large-area low-intensity infrared signals with the top-emissive upconversion device. The semitransparent, large-area, single-pixel upconversion panel can resolve the infrared power density of submicrowatt per centimeter square with Cu:Ag alloy thin film capped with a  $\text{WO}_3$  layer. There is considerable room for improving the AVT of the semitransparent OUD presented in this work, primarily attributed to the donor material that has a shallow frontier molecular orbital than the NFAs. High transparency in favor of visual aesthetic may be achieved with other chemically synthesized donor molecules selectively absorbing infrared wavelengths of interest and other transparent conductive options for the top-emissive electrode.

Image resolution plays a crucial role in whether this technology can be applied in our daily lives, especially for close-eye head-mounted displays. Our previous discussion verified that OUD could fulfill a high-quality infrared image with a maximum resolution of 1588 dots per inch (8). In this work, we have leveraged this



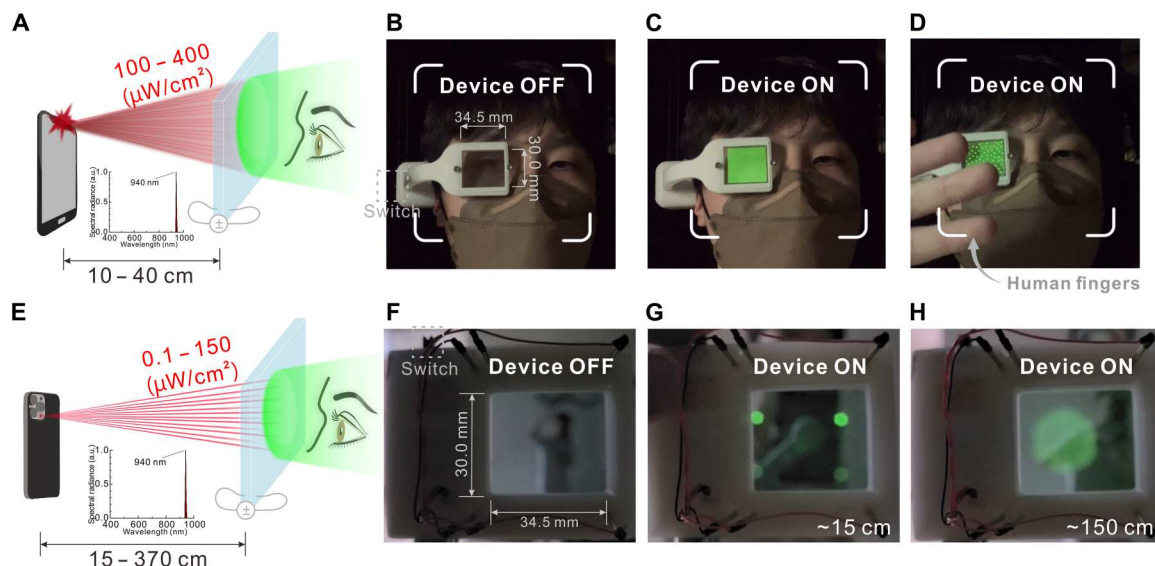


**Fig. 6. Antidetection panels.** (A to D) Infrared visualization (940-nm infrared stimulus) of the facial recognition technology by the wearable, semitransparent, large-area, and single-pixel upconversion panel. (A) Schematic illustration of the antidetection process. The infrared power density changes over the distance between the panel and the front camera system. (B) No signal when the device is off, and the subject's eye can be visualized clearly. (C) Uniform upconversion luminescence visualizes the invisible infrared illumination from the flood illuminator. The subject's eye behind the panel can still be identified. (D) A grid of light dots visualizes the infrared pattern from the dot projector, while the human fingers obstruct part of the infrared flash (flood illuminator). (E to H) Infrared visualization (940-nm infrared stimulus) of the LiDAR function by the upconversion panel. (F) The man standing 3.7-m away waving can be identified through the semitransparent panel. Note that the image focus recording the whole process is locked on the upconversion panel. (G) The flickering infrared pattern is restored to sight by the upconversion panel after switching on the power (the distance between the panel and the camera system is around 15 cm). (H) A single honeycomb infrared pattern is visualized within the frame at a distance of 150 cm away from the light source. The image of the man is clear even behind the upconversion pattern.

advantage to visualize high-density infrared dots from the Face ID or LiDAR system. We found that the light distribution of the incoming signal defines the image resolution rather than the concern over the OUD (cf. Fig. 6H). Application of a spatial filter to achieve a better definition of the infrared pattern in the future could address this issue.

High-detectivity infrared OUD offers an attractive alternative other than the existing techniques of choice that are intrinsically opaque and rigid. The mechanical intractability restricts the crystalline photodiode from economically viable large-area sensing. The semitransparent, large-area, single-pixel upconversion panel demonstrated in this work sheds light on the possibility of visualizing in situ low-intensity infrared signals without a digital camera or optical lenses. The simple, lightweight, wearable antidetection panel opens up a new avenue against the intrusive infrared detection signals in our daily lives and may inspire novel stereoscopic vision applications in the future. It is anticipated that the cost benefits and process flexibility of the pixel-free OUD can support the transition of this technology from bench to reality.

## MATERIALS AND METHODS

### Crude materials and solutions

Zinc acetate di-hydrate [ $\text{Zn}(\text{CH}_3\text{COO})_2 \cdot 2\text{H}_2\text{O}$ , 99%], ethanolamine ( $\text{NH}_2\text{CH}_2\text{CH}_2\text{OH}$ , 99.5%), 2-methoxyethanol ( $\text{CH}_3\text{OCH}_2\text{CH}_2\text{OH}$ , 99.8%), ethanol ( $\text{C}_2\text{H}_5\text{OH}$ , 99.8%), *O*-xylene [ $\text{C}_6\text{H}_4(\text{CH}_3)_2$ , 97%], 1-chloronaphthalene ( $\text{C}_{10}\text{H}_7\text{Cl}$ , technical >85%), and PEIE solution were purchased from Sigma-Aldrich. PTB7-Th and COTIC-4F were purchased from 1-Material. Molybdenum (VI) oxide ( $\text{MoO}_3$ ,

>99.998%), TAPC (>99.5%), BCzPh (>99%),  $\text{Ir}(\text{ppy})_2(\text{acac})$  (>99%), LiF (>99.99%), and the ITO substrates (sheet resistance, 15 ohm  $\square^{-1}$ ) were acquired from Lumtec Corporation. CN-T2T was provided by Shine Materials. The sol-gel ZnO and PEIE solution were prepared and diluted, resembling the previous procedures (26, 46, 47). The donor-acceptor solution was arranged, dissolving PTB7-Th and COTIC-4F (1:1.5, 20 mg  $\text{ml}^{-1}$ ) in *O*-xylene with 2 volume % of 1-chloronaphthalene as an additive.

### Thin-film deposition

The ZnO ETL was developed on ITO-coated glass substrates by first spin-coating at 3000 rpm for 30 s and annealing at 170°C for 20 min, followed by the PEIE solution treatment. A proper amount of the PTB7-Th:COTIC-4F crude solution (40  $\mu\text{l}$  for standard characterization and 200  $\mu\text{l}$  for large-area proof-of-concept demonstration) was then evenly distributed on the ZnO-coated substrate to deposit the desired BHJ blend thickness of 70 nm with the rotation speed of 5500 rpm lasting 40 s. The whole spin-coating BHJ deposition was developed in a nitrogen-filled glove box to prevent any oxygen or humidity. The OPD devices were finalized loading into a thermal evaporator for successive deposition of  $\text{MoO}_3$  (10 nm)/Ag (100 nm) cathode under a  $10^{-6}$  torr base vacuum level. For standard upconversion device, a multilayer light-emissive stacking of TAPC (30 nm)/BCzPh (30 nm)/BCzPh:CN-T2T: $\text{Ir}(\text{ppy})_2(\text{acac})$  (1:1:8% 30 nm)/CN-T2T (25 nm)/CN-T2T:5%  $\text{Li}_2\text{CO}_3$  (5 nm)/Ag (100 nm) was constructed on top of the CGL, while a semitransparent cathode of Cu:Ag (1:50 12 nm)/ $\text{WO}_3$  (30 nm) was chosen for see-through demonstration (32). The active area was defined as 4  $\text{mm}^2$  by the overlapped cathode shadow unless specified.

## Characterization

The photoluminescence spectra (FluoroMax Plus, HORIBA Jobin Yvon), transmittance and absorption spectra (V-770, Jasco), EQE spectra (QE-R3011, Enlitech), and LDR measurement were performed following previous protocols (8). However, the photoelectrical characteristics of the standard structure were recorded using a spectrometer (LQ-100R, Enlitech) from an integrated sphere system equipped with a photomultiplier tube (PMT) and a power source meter (B2901A, Keysight) (18). The 940-nm infrared laser (MLL-III-940, CNI) was coupled into the integrated sphere calibrated by a power meter (1918-R, Newport) and a silicon optical power detector (818-SL, Newport) with National Institute of Standards and Technology traceability. The 750-nm short-pass filters (15-262, Edmund Optics) were prepared for the sensitive PMT to accurately capture the electroluminescence spectra avoiding the undesired saturation by the high-intensity laser. Infrared-to-visible upconversion efficiency can then be evaluated according to the following equation

$$\eta_{p-p} (\%) = \frac{\# \text{ photon}_{\text{VIS}}}{\# \text{ photon}_{\text{NIR}}} = \int \frac{\lambda_{\text{up}} I_{\text{up}}(\lambda)}{hc} d\lambda / \frac{\lambda_{\text{inc}} P_{\text{inc}}}{hc}$$

$$= \frac{\# \text{ electron}}{\frac{\lambda_{\text{inc}} P_{\text{inc}}}{hc}} \times \frac{\int \frac{\lambda_{\text{up}} I_{\text{up}}(\lambda)}{hc} d\lambda}{\# \text{ electron}} \quad (1)$$

which describes the utilization rate of incoming infrared photons for visible photons (48, 49).  $h$  and  $c$  are the Planck constant and the speed of light in the vacuum.  $\lambda_{\text{up}}$  and  $I_{\text{up}}(\lambda)$  are the out-coupled visible wavelength and corresponding intensity.  $\lambda_{\text{inc}}$  and  $P_{\text{inc}}$  are the incident infrared wavelength and the related irradiation power of interest. Note that a mask (2.27 mm<sup>2</sup> opening) was placed on the device to define the active area exclusively. The mask size was ascertained by the optical microscope (BX53F2, Olympus), and the opening area was calculated by ImageJ (fig. S8). The OUD should perform an absolute off state under the bias without infrared stimulus that any leakage luminance was considered background noise, accounting for inaccurate calculation regarding the upconversion process of the infrared contribution. To precisely report the  $\eta_{p-p}$  against overestimation, the upper limit of the upconversion luminance was recorded at the bias where the leakage luminance showed less than 0.1 cd m<sup>-2</sup> in the absence of infrared stimulus throughout the work. The photon-to-electron or electron-to-photon rate can be extracted by calculating the photoinduced electron number with  $\# \text{electron} = (I_{\text{photo}} - I_{\text{dark}})/q$ , where  $q$  is the elementary charge.

## Semitransparent, large-area, single-pixel panel Infrared viewing sensor

The infrared power density on the active area was attenuated by directly controlling the LED current (M940L3, Thorlabs) with the control panel (DC2200, Thorlabs), calibrated by the power meter (1918-R, Newport) and a silicon power detector (818-SL, Newport) in advance.

## Face ID antidection

We covered the subject's face with the mask and proceeded under weak ambient light (<10 lux, 5700 K) instead of following the on-screen instructions. The dim ambient light could induce more infrared illumination from the flood illuminator (940 nm; power density, 100 to 400  $\mu\text{W cm}^{-2}$ ; distance, 10 to 40 cm), with intensity

determined by the proximity sensor and ambient light sensor. The built-in screen recording function (iPhone XR) recorded the complete upconversion process (movie S1).

## LiDAR antidection

We activated the LiDAR function using the native Measure app of the smartphone. The infrared intensity from the rear camera (iPhone 12 Pro) was attenuated by gradually increasing the distance between the panel and the smartphone. The whole procedure was also recorded with the built-in screen recording function (movie S2).

## Supplementary Materials

### This PDF file includes:

Supplementary Text

Figs. S1 to S8

Table S1

Legends for movies S1 and S2

### Other Supplementary Material for this

### manuscript includes the following:

Movies S1 and S2

## REFERENCES AND NOTES

- Z. Hu, C. Fang, B. Li, Z. Zhang, C. Cao, M. Cai, S. Su, X. Sun, X. Shi, C. Li, T. Zhou, Y. Zhang, C. Chi, P. He, X. Xia, Y. Chen, S. S. Gambhir, Z. Cheng, J. Tian, First-in-human liver-tumour surgery guided by multispectral fluorescence imaging in the visible and near-infrared-II windows. *Nat. Biomed. Eng.* **4**, 259–271 (2020).
- J.-E. Kallhammer, The road ahead for car night-vision. *Nat. Photonics.* **5**, 12–13 (2006).
- S. Goossens, G. Navickaite, C. Monasterio, S. Gupta, J. J. Piqueras, R. Pérez, G. Burwell, I. Nikitskiy, T. Lasanta, T. Galán, E. Puma, A. Centeno, A. Pesquera, A. Zurutuza, G. Konstantatos, F. Koppens, Broadband image sensor array based on graphene-CMOS integration. *Nat. Photon.* **11**, 366–371 (2017).
- C.-J. Shih, Y.-M. Huang, J.-J. Sze, T.-T. Wu, F.-S. Guo, W.-C. Hsu, T.-H. Tseng, K. Liao, C.-C. Kuo, T.-H. Chen, W.-C. Chiang, C.-H. Chuang, K.-Y. Chou, C.-H. Chung, K.-Y. Chou, C.-H. Tseng, C.-J. Wang, D.-N. Young, A 45 nm stacked CMOS image sensor process technology for submicron pixel. *Sensors.* **17**, 2816 (2017).
- S. Fuentes-Hernandez, W.-F. Chou, T. M. Khan, L. Diniz, J. Lukens, F. A. Larrain, V. A. Rodríguez-Toro, B. Kippelen, Large-area low-noise flexible organic photodiodes for detecting faint visible light. *Science* **370**, 698–701 (2020).
- S.-H. Lee, A. R. bin Mohd Yusoff, C. Lee, S. C. Yoon, Y.-Y. Noh, Toward color-selective printed organic photodetectors for high-resolution image sensors: From fundamentals to potential commercialization. *Mater. Sci. Eng. R Rep.* **147**, 100660 (2022).
- J. Chen, J. Tao, D. Ban, M. G. Helander, Z. Wang, J. Qiu, Z. Lu, Hybrid organic/inorganic optical up-converter for pixel-less near-infrared imaging. *Adv. Mater.* **24**, 3138–3142 (2012).
- C.-J. Shih, Y.-Z. Li, M.-Z. Li, S. Biring, B.-C. Huang, C.-W. Liu, T.-H. Yeh, D. Luo, J.-H. Lee, Y.-H. Huang, K.-T. Wong, S.-W. Liu, Transparent organic upconversion device targeting high-grade infrared visual image. *Nano Energy* **86**, 106043 (2021).
- D. Y. Kim, T.-H. Lai, J. W. Lee, J. R. Manders, F. So, Multi-spectral imaging with infrared sensitive organic light emitting diode. *Sci. Rep.* **4**, 5946 (2014).
- S.-W. Liu, C.-C. Lee, C.-H. Yuan, W.-C. Su, S.-Y. Lin, W.-C. Chang, B.-Y. Huang, C.-F. Lin, Y.-Z. Lee, T.-H. Su, K.-T. Chen, Transparent organic upconversion devices for near-infrared sensing. *Adv. Mater.* **27**, 1217–1222 (2015).
- H. Tachibana, N. Aizawa, Y. Hidaka, T. Yasuda, Tunable full-color electroluminescence from all-organic optical upconversion devices by near-infrared sensing. *ACS Photonics.* **4**, 223–227 (2017).
- D. Yang, X. Zhou, D. Ma, A. Vadim, T. Ahamad, S. M. Alshehri, Near infrared to visible light organic up-conversion devices with photon-to-photon conversion efficiency approaching 30%. *Mater. Horiz.* **5**, 874–882 (2018).
- K. Strassel, A. Kaiser, S. Jenatsch, A. C. Véron, S. B. Anantharaman, E. Hack, M. Diethelm, F. Nüesch, R. Aderne, C. Legnani, S. Yakunin, M. Cremona, R. Hany, Squaraine dye for a visibly transparent all-organic optical upconversion device with sensitivity at 1000 nm. *ACS Appl. Mater. Interfaces* **10**, 11063–11069 (2018).

14. N. Li, Z. Lan, Y. S. Lau, J. Xie, D. Zhao, F. Zhu, SWIR photodetection and visualization realized by incorporating an organic SWIR sensitive bulk heterojunction. *Adv. Sci.* **7**, 2000444 (2020).
15. C.-H. Yuan, C.-C. Lee, C.-F. Liu, Y.-H. Lin, W.-C. Su, S.-Y. Lin, K.-T. Chen, Y.-D. Li, W.-C. Chang, Y.-Z. Li, T.-H. Su, Y.-H. Liu, S.-W. Liu, Cathodic-controlled and near-infrared organic up-converter for local blood vessels mapping. *Sci. Rep.* **6**, 32324 (2016).
16. N. Li, N. Eedugurala, D. Leem, J. D. Azoulay, T. N. Ng, Organic upconversion imager with dual electronic and optical readouts for shortwave infrared light detection. *Adv. Funct. Mater.* **31**, 2100565 (2021).
17. X. Du, J. Han, Z. He, C. Han, X. Wang, J. Wang, Y. Jiang, S. Tao, Efficient organic upconversion devices for low energy consumption and high-quality noninvasive imaging. *Adv. Mater.* **33**, 2102812 (2021).
18. W. Zhou, Y. Shang, F. P. García de Arquer, K. Xu, R. Wang, S. Luo, X. Xiao, X. Zhou, R. Huang, E. H. Sargent, Z. Ning, Solution-processed upconversion photodetectors based on quantum dots. *Nat. Electron.* **3**, 251–258 (2020).
19. S.-H. Liao, H.-J. Jhuo, Y.-S. Cheng, S.-A. Chen, Fullerene derivative-doped zinc oxide nanofilm as the cathode of inverted polymer solar cells with low-bandgap polymer (PTB7-Th) for high performance. *Adv. Mater.* **25**, 4766–4771 (2013).
20. J. Hou, O. Inganäs, R. H. Friend, F. Gao, Organic solar cells based on non-fullerene acceptors. *Nat. Mater.* **17**, 119–128 (2018).
21. J. Yuan, Y. Zhang, L. Zhou, G. Zhang, H.-L. Yip, T.-K. Lau, X. Lu, C. Zhu, H. Peng, P. A. Johnson, M. Leclerc, Y. Cao, J. Ulanski, Y. Li, Y. Zou, Single-junction organic solar cell with over 15% efficiency using fused-ring acceptor with electron-deficient core. *Joule*. **3**, 1140–1151 (2019).
22. N. Li, Y. S. Lau, Z. Xiao, L. Ding, F. Zhu, NIR to visible light upconversion devices comprising an NIR charge generation layer and a perovskite emitter. *Adv. Opt. Mater.* **6**, 1801084 (2018).
23. S. Holliday, R. S. Ashraf, A. Wadsworth, D. Baran, S. A. Yousaf, C. B. Nielsen, C.-H. Tan, S. D. Dimitrov, Z. Shang, N. Gasparini, M. Alamoudi, F. Laquai, C. J. Brabec, A. Salleo, J. R. Durrant, I. McCulloch, High-efficiency and air-stable P3HT-based polymer solar cells with a new non-fullerene acceptor. *Nat. Commun.* **7**, 11585 (2016).
24. J. Lee, S.-J. Ko, M. Seifrid, H. Lee, B. R. Luginbuhl, A. Karki, M. Ford, K. Rosenthal, K. Cho, T. Nguyen, G. C. Bazan, Bandgap narrowing in non-fullerene acceptors: Single atom substitution leads to high optoelectronic response beyond 1000 nm. *Adv. Energy Mater.* **8**, 1801212 (2018).
25. J. Lee, S.-J. Ko, H. Lee, J. Huang, Z. Zhu, M. Seifrid, J. Vollbrecht, V. V. Brus, A. Karki, H. Wang, K. Cho, T.-Q. Nguyen, G. C. Bazan, Side-chain engineering of nonfullerene acceptors for near-infrared organic photodetectors and photovoltaics. *ACS Energy Lett.* **4**, 1401–1409 (2019).
26. Y.-M. Sung, A. K. Akbar, S. Biring, C.-F. Li, Y.-C. Huang, S.-W. Liu, The effect of ZnO preparation on the performance of inverted polymer solar cells under one sun and indoor light. *J. Mater. Chem.* **9**, 1196–1204 (2021).
27. K.-G. Lim, S. Ahn, T.-W. Lee, Energy level alignment of dipolar interface layer in organic and hybrid perovskite solar cells. *J. Mater. Chem.* **6**, 2915–2924 (2018).
28. C.-C. Lee, S. Biring, S.-J. Ren, Y.-Z. Li, M.-Z. Li, N. R. Al Amin, S.-W. Liu, Reduction of dark current density in organic ultraviolet photodetector by utilizing an electron blocking layer of TAPC doped with MoO<sub>3</sub>. *Org. Electron.* **65**, 150–155 (2019).
29. M. Wang, Y.-H. Huang, K.-S. Lin, T.-H. Yeh, J. Duan, T.-Y. Ko, S.-W. Liu, K.-T. Wong, B. Hu, Revealing the cooperative relationship between spin, energy, and polarization parameters toward developing high-efficiency exciplex light-emitting diodes. *Adv. Mater.* **31**, 1904114 (2019).
30. N. R. A. Amin, K. K. Kesavan, S. Biring, C.-C. Lee, T.-H. Yeh, T.-Y. Ko, S.-W. Liu, K.-T. Wong, A comparative study via photophysical and electrical characterizations on interfacial and bulk exciplex-forming systems for efficient organic light-emitting diodes. *ACS Appl. Electron. Mater.* **2**, 1011–1019 (2020).
31. S.-W. Liu, Y.-Z. Li, S.-Y. Lin, Y.-H. Li, C.-C. Lee, Inducing the trap-site in an emitting-layer for an organic upconversion device exhibiting high current-gain ratio and low turn-on voltage. *Org. Electron.* **30**, 275–280 (2016).
32. M.-Z. Li, C.-C. Lee, S. Biring, I.-S. Hsu, D. Luo, R. Estrada, Y.-S. Wu, C.-C. Yang, S.-W. Liu, Vacuum-deposited transparent organic photovoltaics for efficiently harvesting selective ultraviolet and near-infrared solar energy. *Solar RRL* **5**, 2000564 (2020).
33. S. Ryu, N. Y. Ha, Y. H. Ahn, J.-Y. Park, S. Lee, Light intensity dependence of organic solar cell operation and dominance switching between Shockley–Read–Hall and bimolecular recombination losses. *Sci. Rep.* **11**, 16781 (2021).
34. J. Kublitski, A. Hofacker, B. K. Boroujeni, J. Benduhn, V. C. Nikolis, C. Kaiser, D. Spoltore, H. Kleemann, A. Fischer, F. Ellinger, K. Vandewal, K. Leo, Reverse dark current in organic photodetectors and the major role of traps as source of noise. *Nat. Commun.* **12**, 551 (2021).
35. Y. Fang, A. Armin, P. Meredith, J. Huang, Accurate characterization of next-generation thin-film photodetectors. *Nat. Photon.* **13**, 1–4 (2018).
36. J. Vollbrecht, J. Lee, S.-J. Ko, V. V. Brus, A. Karki, W. Le, M. Seifrid, M. J. Ford, K. Cho, G. C. Bazan, T.-Q. Nguyen, Design of narrow bandgap non-fullerene acceptors for photovoltaic applications and investigation of non-geminate recombination dynamics. *J. Mater. Chem.* **8**, 15175–15182 (2020).
37. P. Hartnagel, T. Kirchartz, Understanding the light-intensity dependence of the short-circuit current of organic solar cells. *Adv. Theory Simul.* **3**, 2000116 (2020).
38. Y. Fang, J. Huang, Resolving weak light of sub-picowatt per square centimeter by hybrid perovskite photodetectors enabled by noise reduction. *Adv. Mater.* **27**, 2804–2810 (2015).
39. M. Wang, D. Luo, T.-H. Yeh, Y.-H. Huang, C.-L. Ko, W.-Y. Hung, Y. Tang, S.-W. Liu, K.-T. Wong, B. Hu, Extending anisotropy dynamics of light-emitting dipoles as necessary condition toward developing highly-efficient OLEDs. *Adv. Opt. Mater.*, 2202477 (2023).
40. B. H. Yu, Y. Cheng, M. Li, S.-W. Tsang, F. So, Sub-band gap turn-on near-infrared-to-visible up-conversion device enabled by an organic–inorganic hybrid perovskite photovoltaic absorber. *ACS Appl. Mater. Interfaces* **10**, 15920–15925 (2018).
41. J. Vollbrecht, V. V. Brus, S.-J. Ko, J. Lee, A. Karki, D. X. Cao, K. Cho, G. C. Bazan, T.-Q. Nguyen, Quantifying the nongeminate recombination dynamics in nonfullerene bulk heterojunction organic solar cells. *Adv. Energy Mater.* **9**, 1901438 (2019).
42. M. Pranav, J. Benduhn, M. Nyman, S. M. Hosseini, J. Kublitski, S. Shoaee, D. Neher, K. Leo, D. Spoltore, Enhanced charge selectivity via anodic-C<sub>60</sub> layer reduces nonradiative losses in organic solar cells. *ACS Appl. Mater. Interfaces* **13**, 12603–12609 (2021).
43. H. Yu, D. Kim, J. Lee, S. Baek, J. Lee, R. Singh, F. So, High-gain infrared-to-visible upconversion light-emitting phototransistors. *Nat. Photon.* **10**, 129–134 (2016).
44. W. Hu, C. Vael, M. Diethelm, K. Strassel, S. B. Anantharaman, A. Aribia, M. Cremona, S. Jenatsch, F. Nüesch, R. Hany, On the response speed of narrowband organic optical upconversion devices. *Adv. Opt. Mater.* **10**, 2200695 (2022).
45. H. J. Snaith, The perils of solar cell efficiency measurements. *Nat. Photon.* **6**, 337–340 (2012).
46. H.-C. Cha, Y.-C. Huang, F.-H. Hsu, C.-M. Chuang, D.-H. Lu, C.-W. Chou, C.-Y. Chen, C.-S. Tsao, Performance improvement of large-area roll-to-roll slot-die-coated inverted polymer solar cell by tailoring electron transport layer. *Sol. Energy Mater. Sol. Cells* **130**, 191–198 (2014).
47. Y.-C. Huang, D.-H. Lu, C.-F. Li, C.-W. Chou, H.-C. Cha, C.-S. Tsao, Printed silver grid incorporated with PEIE doped ZnO as an auxiliary layer for high-efficiency large-area sprayed organic photovoltaics. *IEEE J. Photovolt.* **9**, 1297–1301 (2019).
48. X. Chu, M. Guan, L. Niu, Y. Zeng, Y. Li, Y. Zhang, Z. Zhu, B. Wang, Fast Responsive and highly efficient optical upconverter based on phosphorescent OLED. *ACS Appl. Mater. Interfaces* **6**, 19011–19016 (2014).
49. S.-J. He, D.-K. Wang, Z.-X. Yang, J.-X. Man, Z.-H. Lu, Integrated tandem device with photoactive layer for near-infrared to visible upconversion imaging. *Appl. Phys. Lett.* **112**, 243301 (2018).

**Acknowledgments:** S.-W.L. is grateful to H.-H. Wu, Syskey Technology Co. Ltd. (Taiwan) for assistance in designing the fabrication system. **Funding:** This work was supported by Ministry of Science and Technology Taiwan grant nos. MOST 110-2221-E-131-010, MOST 110-2622-E-131-011, MOST 110-2221-E-131-019, MOST 111-2221-E-131-013, MOST 110-2222-E-002-003-MY3, and MOST 109-2223-E-131-001-MY3. **Author contributions:** Conceptualization: C.-J.S. and S.-W.L. Data curation: C.-J.S. and T.-Y.W. Formal analysis: C.-J.S. Investigation: C.-J.S., T.-Y.W., and C.-W.Y. Supervision: Y.-C.H., J.-H.L., and S.-W.L. Visualization: C.-J.S., I.-S.H., A.K.A., and J.-Y.L. Writing (original draft): C.-J.S. Writing (review and editing): C.-J.S., S.B., J.-H.L., and S.-W.L. **Competing interests:** The authors declare that they have no competing interests. **Data and materials availability:** All data needed to evaluate the conclusions in the paper are present in the paper and/or the Supplementary Materials.

Submitted 1 July 2022  
Accepted 23 March 2023  
Published 26 April 2023  
10.1126/sciadv.add7526

## Transparent organic upconversion devices displaying high-resolution, single-pixel, low-power infrared images perceived by human vision

Chun-Jen Shih, Yu-Ching Huang, Tai-Yung Wang, Chang-Wei Yu, I-Sheng Hsu, Abdul Khalik Akbar, Jai-Yi Lin, Sajal Biring, Jiun-Haw Lee, and Shun-Wei Liu

*Sci. Adv.*, **9** (17), eadd7526.  
DOI: 10.1126/sciadv.add7526

### View the article online

<https://www.science.org/doi/10.1126/sciadv.add7526>

### Permissions

<https://www.science.org/help/reprints-and-permissions>

Use of this article is subject to the [Terms of service](#)

---

*Science Advances* (ISSN ) is published by the American Association for the Advancement of Science. 1200 New York Avenue NW, Washington, DC 20005. The title *Science Advances* is a registered trademark of AAAS.  
Copyright © 2023 The Authors, some rights reserved; exclusive licensee American Association for the Advancement of Science. No claim to original U.S. Government Works. Distributed under a Creative Commons Attribution NonCommercial License 4.0 (CC BY-NC).